

J-MoDL: Joint Model-Based Deep Learning for Optimized Sampling and Reconstruction

Hemant Kumar Aggarwal, *Member, IEEE*, Mathews Jacob, *Senior Member, IEEE*,

Abstract—Modern MRI schemes, which rely on compressed sensing or deep learning algorithms to recover MRI data from undersampled multichannel Fourier measurements, are widely used to reduce scan time. The image quality of these approaches is heavily dependent on the sampling pattern. We introduce a continuous strategy to jointly optimize the sampling pattern and the parameters of the reconstruction algorithm. We propose to use a model-based deep learning (MoDL) image reconstruction algorithm, which alternates between a data consistency module and a convolutional neural network (CNN). We use a multi-channel forward model, consisting of a non-uniform Fourier transform with continuously defined sampling locations, to realize the data consistency block. This approach facilitates the joint and continuous optimization of the sampling pattern and the CNN parameters. We observe that the joint optimization of the sampling patterns and the reconstruction module significantly improves the performance, compared to current deep learning methods that use variable density sampling patterns. Our experiments show that the improved decoupling of the CNN parameters from the sampling scheme offered by the MoDL scheme translates to improved optimization and performance compared to a similar scheme using a direct-inversion based reconstruction algorithm. The experiments also show that the proposed scheme offers good convergence and reduces the dependence on initialization.

Index Terms—Sampling, Deep learning, Parallel MRI

I. INTRODUCTION

MRI imaging offers several benefits, including good soft-tissue contrast, non-ionizing radiation, and the availability of multiple tissue contrasts. However, its main limitation is the slow image acquisition rate. The last decade has witnessed several approaches, including parallel MRI and compressed sensing, to recover the images from undersampled k-space measurements to overcome the above challenge. The reconstruction quality heavily depends on the specific sampling pattern used to acquire the data, the regularization priors, as well as the hyperparameters. Early parallel MRI hardware [1] was designed to eliminate the need to sample adjacent k-space samples, making uniform undersampling of k-space a desirable approach. By contrast, compressed sensing [2], [3] advocates for the sampling pattern to be maximally incoherent. Since the k-space center is associated with high energy, variable density schemes that sample the center with a higher density are preferred by practitioners. One of the standard practices is the Poisson-disc variable

density approach, which is a heuristic that combines the above intuitions [4].

The computational optimization of sampling patterns has a long history in MRI. The current solutions can be broadly classified as algorithm-dependent and algorithm-agnostic. The algorithm-agnostic approaches such as [5]–[8] consider specific image properties and optimize the sampling patterns to improve the measurement diversity for that class. Image properties, including image support [5], parallel acquisition using sensitivity encoding (SENSE) [6], [8], [9], and sparsity constraints [7] have been introduced. These experiment design strategies often rely on the Cramer-Rao (CR) bound, assuming the knowledge of the image support or location of the sparse coefficients. Algorithm-dependent schemes such as [10], [11] optimize the sampling pattern, assuming specific reconstruction algorithms (e.g., TV or wavelet sparsity). These approaches [10], [11] only consider single-channel settings with undersampled Fourier transform as a forward model. They utilize a subset of discrete sampling locations using greedy or continuous optimization strategies to minimize the reconstruction error. The TV or sparse optimization algorithms produce reconstructed images in an inner loop to provide a measure of image quality. The main challenge with both of the above approaches (algorithm-dependent and agnostic) is the high computational complexity (e.g. run times of several days), when applied to a large class of images or multi-dimensional imaging problems. In many cases, the optimization is performed over very few images. Moreover, the parameters of the reconstruction algorithm are assumed to be fixed during the optimization process.

Deep learning methods, which offer significantly improved computational efficiency and higher image quality, are emerging as powerful algorithms for the reconstruction of undersampled k-space data. Direct inversion methods that use a convolutional neural network (CNN) to recover the images from the undersampled data directly [12], [13] and model-based methods [14]–[19], which formulate the recovery as a regularized optimization scheme, have been studied extensively. Early empirical studies suggest that incoherent sampling patterns, which are widely used in compressed sensing, may not be necessary for good reconstruction performance in this setting [15]. Unlike classical methods that rely on specific image properties (e.g. sparsity, support-constraints), the non-linear convolutional neural networks (CNN) schemes exploit complex non-linear redundancies that exist in images. This makes it difficult to use the algorithm-agnostic computational optimization algorithms discussed above. Besides, the learned CNN parameters often may be strongly coupled to

Hemant Kumar Aggarwal (email: hemantkumar-aggarwal@uiowa.edu) and Mathews Jacob (email: mathews-jacob@uiowa.edu) are with the Department of Electrical and Computer Engineering, University of Iowa, IA, USA, 52242.

Manuscript received Month day, year; revised Month day, year.

This work is supported by 1R01EB019961-01A1. This work was conducted on an MRI instrument funded by 1S10OD025025-01

the specific sampling scheme. Hence, a joint strategy, which simultaneously optimizes for the acquisition scheme as well as the reconstruction algorithm, is necessary to obtain the best performance.

Fortunately, the significantly reduced computational complexity of deep learning reconstruction algorithms makes it possible to perform the joint optimization. For instance, the recent LOUPE algorithm [20] jointly optimizes the sampling density in k-space and the reconstruction algorithm. Since this scheme seeks to optimize the sampling density rather than the sampling locations, it may be difficult for this scheme to capitalize on the complex phase dependencies (e.g. conjugate symmetry) between the k-space samples. The approaches in [21], [22] instead consider a sampling mask to choose a subset of Cartesian samples, which is optimized. A challenge with [22] is that the final sampling pattern heavily depends on the initialization of the pattern. This may be attributed to the complex nature of the optimization landscape, consisting of several local minima. Note that the CNN in a direct-inversion scheme essentially performs the inverse of the forward model; the strong coupling between the CNN parameters and the specific sampling patterns can result in a complex optimization landscape. We note that another class of deep learning solutions involve active strategies [23], [24], where a neural network is used to predict the next k-space sample to be acquired based on the image reconstructed from the current samples. We do not focus on such active paradigms in this work.

The main focus of this work is to jointly optimize the sampling pattern and the deep network parameters for parallel MRI reconstruction. Most of the previous optimization strategies [10], [11], [20]–[22] are only restricted to the single-channel setting. We rely on an algorithm-dependent strategy to search for the best sampling pattern in the multichannel setting. The main difference of the proposed scheme from [10], [11], [20], [21] is that we do not constrain the sampling pattern to be a subset of the Cartesian sampling pattern. Specifically, we assume the sampling locations to be continuous variables. Since the derivatives with respect to the sampling locations are well-defined, we propose to optimize the sampling locations continuously. We rely on the model-based deep learning (MoDL) strategy to improve the optimization landscape, which helps in reducing the local minima problems. We note that the CNN module in MoDL primarily captures the image properties and is relatively less dependent on the sampling patterns, compared to the direct-inversion schemes. We hypothesize that the reduced coupling between the CNN parameters and the acquisition scheme results in a simpler optimization landscape, which reduces the impact of local minima problems. To further improve the landscape, we additionally parameterize the sampling patterns to reduce the dimension of the search space. The fast inversion offered by MoDL facilitates the training of the algorithm using several images, thus improving the generalization performance of the learned sampling pattern.

II. METHOD

A. Image Formation

We consider the recovery of the complex image $\rho \in \mathbb{C}^{M \times N}$ from its non-Cartesian Fourier samples:

$$b[i, j] = \sum_{\mathbf{m} \in \mathbb{Z}^2} s_j[\mathbf{m}] \rho[\mathbf{m}] e^{-j\mathbf{k}_i^T \mathbf{m}} + n[i, j], \mathbf{k}_i \in \Theta. \quad (1)$$

Here, Θ is a set of sampling locations and $n[i, j]$ is the noise process. $s_j; j = 1, \dots, J$ corresponds to the sensitivity of the j^{th} coil, while \mathbf{k}_i is the i^{th} sampling location. The above mapping can be compactly represented as $\mathbf{b} = \mathcal{A}_\Theta(\rho) + \mathbf{n}$. The measurement operator \mathcal{A}_Θ is often termed to as the forward model. It captures the information about the sampling pattern as well as the receive coil sensitivities. We note that the forward model is often modified to include additional information about the imaging physics, including field inhomogeneity distortions and relaxation effects [25].

B. Regularized Image recovery

Model-based algorithms are widely used for the recovery of images from heavily undersampled measurements, such as (1). These schemes pose the reconstruction as an optimization problem of the form

$$\hat{\rho}_{\{\Theta, \Phi\}} = \arg \min_{\rho} \|\mathbf{b} - \mathcal{A}_\Theta(\rho)\|_2^2 + \mathcal{R}_\Phi(\rho). \quad (2)$$

Here, \mathcal{R}_Φ is a regularization penalty. Regularizers include transform domain sparsity [26], total variation regularization [27], and structured low-rank methods [28]. For instance, in transform domain sparsity, the regularizer is chosen as $\mathcal{R}(\rho) = \lambda \|\mathbf{T}\rho\|_{\ell_1}$ with $\Phi = \{\lambda, \mathbf{T}\}$ denoting the parameters of the regularizer and the transform. We rely on the notation $\hat{\rho}_{\{\Theta, \Phi\}}$ for the solution of (2) to denote its dependence on the regularization parameters as well as the sampling pattern.

C. Deep learning based image recovery

Deep learning methods are increasingly being investigated as alternatives for regularized image reconstruction. Instead of algorithms that rely on the hand-crafted priors discussed above, these schemes learn the parameters from exemplar data. Hence, these schemes are often termed as data-driven methods.

1) *Direct-inversion schemes:* Direct-inversion schemes [12], [13] rely on a deep CNN \mathcal{N}_Φ to recover the images from undersampled gridding reconstruction $\mathcal{A}_\Theta^H(\mathbf{b})$ as

$$\rho_{\text{direct}} = \mathcal{N}_\Phi \left(\mathcal{A}_\Theta^H(\mathbf{b}) \right). \quad (3)$$

Here Φ denotes the learnable parameters of the CNN \mathcal{N}_Φ (see Fig. 1(a)). The CNN parameters are closely coupled with the sampling pattern Θ to facilitate the recovery of images in a specific class. Large networks are often needed in this setting to learn the inverse of \mathcal{A}_Θ over the image class, which implies that large training datasets are often needed to learn a large number of parameters.

2) *Model-based deep learning*: Model-based deep learning (MoDL) [14] rely on a formulation similar to (2), where the hand-crafted image regularization penalties in (2) are replaced with learned priors; image recovery is formulated as

$$\hat{\rho}_{\{\Theta, \Phi\}} = \arg \min_{\rho} \|\mathbf{b} - \mathcal{A}_{\Theta}(\rho)\|_2^2 + \|\rho - \mathcal{D}_{\Phi}(\rho)\|_F^2, \quad (4)$$

where \mathcal{D}_{Φ} is a residual learning based CNN that is designed to extract the noise and alias terms in ρ . The optimization problem specified by (4) is solved using an iterative algorithm, which alternates between a denoising step and a data-consistency step

$$\rho_{n+1} = \left(\mathcal{A}_{\Theta}^H \mathcal{A}_{\Theta} + \mathcal{I} \right)^{-1} \left(\mathbf{z}_n + \mathcal{A}_{\Theta}^H \mathbf{b} \right) \quad (5)$$

$$\mathbf{z}_{n+1} = \mathcal{D}_{\Phi}(\rho_{n+1}). \quad (6)$$

Here, (5) is implemented using a conjugate gradients algorithm. This iterative algorithm is unrolled to obtain a deep recursive network $\mathcal{M}_{\Theta, \Phi}$, where the weights of the CNN blocks and data consistency blocks are shared across iterations as shown in Fig. 1(b). Specifically, the solution to (4) is given by

$$\hat{\rho}_{\Theta, \Phi} = \mathcal{M}_{\Theta, \Phi}(\mathcal{A}_{\Theta}(\rho)). \quad (7)$$

Thus, the main distinction between MoDL and direct-inversion scheme is the structure of the network $\mathcal{M}_{\Theta, \Phi}$. Since the data consistency block is used within MoDL, considerably smaller CNNs \mathcal{D}_{Φ} are sufficient in the MoDL setting. Specifically, the network parameters are shared across iterations. The fewer number of parameters translates to a significantly lower amount of required training data [14].

D. Optimization of sampling patterns and hyperparameters

The focus of this work is to optimize the sampling pattern specified by Θ in (1) and the parameters of the reconstruction algorithm (2) to improve the quality of the reconstructed images. Conceptually, the regularization priors encourage the solution to be restricted to a family of feasible images (e.g. wavelet representation with few sparse coefficients). The objective is to optimize the sampling pattern to capture information that is maximally complementary to the image representation.

Early approaches that rely on compressed sensing algorithms [10], [11] optimize the sampling pattern Θ such that

$$\{\Theta^*\} = \arg \min_{\Theta} \sum_{i=1}^N \|\hat{\rho}_{i, \{\Theta, \Phi\}} - \rho_i\|_2^2, \quad (8)$$

is minimized. Here $\rho_i; i = 1, \dots, N$ are the different training images used in the optimization process and $\hat{\rho}_{i, \{\Theta, \Phi\}}$ are the corresponding reconstructed images, recovered using (2). Greedy [11] or continuous optimization schemes [10] are used to solve (8). However, the main challenge associated with these schemes is the high complexity of the optimization algorithm used to solve (2). Note that the optimization scheme (2) is in the inner loop; for each sampling pattern, the N images have to be reconstructed using computationally expensive CS methods to have the energy defined. This makes it challenging to train the pattern using a large batch of training images. Usually, the

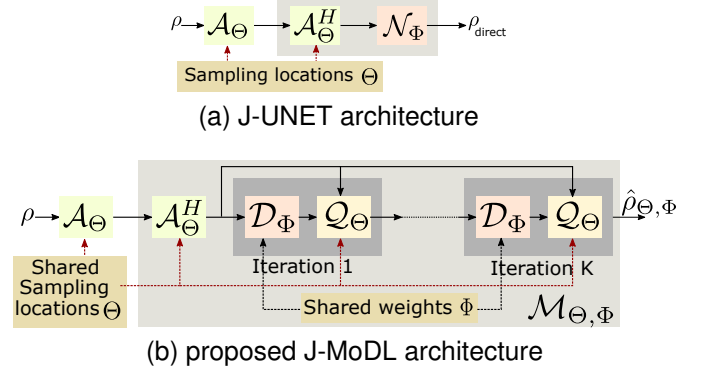


Fig. 1. Illustration of the simultaneous sampling and reconstruction architectures. (a) The direct-inversion (J-UNET) architecture described by (3), where a CNN \mathcal{N}_{Φ} is used to recover the images from $\mathcal{A}_{\Theta}^H \mathbf{b}$. As discussed previously, the CNN parameters are closely coupled with the specific sampling pattern, making joint optimization challenging. (b) corresponds to the J-MoDL architecture, described by (5) and (6). Each iteration alternates between the CNN denoiser \mathcal{D}_{Φ} and the data-consistency block \mathcal{Q}_{Θ} . The data consistency block \mathcal{Q}_{Θ} inverts the measured Fourier samples assuming \mathbf{z}_n , while \mathcal{D}_{Φ} acts as a *denoiser* of the current iterate. The blocks \mathcal{D}_{Φ} and \mathcal{Q}_{Θ} are relatively independent of Θ and Φ , respectively.

hyperparameters of the algorithm denoted by Φ are assumed to be fixed during this optimization.

The fast image recovery offered by deep learning methods such as LOUPE [20] and PILOT [22] offer an alternative to accelerate (8) and simultaneously solve for the hyperparameters Φ . Instead of directly solving for the k-space locations, the LOUPE approach optimizes for the sampling density [20]. Specifically, they assume the k-space sampling locations that are acquired to be binary random variables $\mathbf{k}_i \sim \mathcal{B}(p_i)$ and optimize for the probabilities p_i . They rely on several random realizations of \mathbf{k}_i and the corresponding reconstructions to perform the optimization. Note that this is a relaxation of the original problem. Since the density may not capture the dependencies between k-space samples (e.g., conjugate symmetry when the image is real or smoothly varying phase), improved gains may be obtained by directly solving for the k-space sampling locations rather than the density, such that the ℓ_2 training error is minimized in PILOT [22]

$$\{\Theta^*, \Phi^*\} = \arg \min_{\Theta, \Phi} \sum_{i=1}^N \|\mathcal{N}_{\Phi}(\mathcal{A}_{\Theta}(\rho_i)) - \mathbf{x}_i\|_2^2, \quad (9)$$

where \mathcal{N}_{Φ} is specified by a direct-inversion network (3). A challenge with the PILOT scheme is the heavy dependence of the final sampling pattern Θ^* on the initialization. We hypothesize that this dependence is because of the complex optimization landscape with multiple local minima, resulting in the algorithm converging to a local minimum close to the initialization.

E. Proposed Joint Optimization Strategy

This work proposes joint model-based deep learning (J-MoDL) framework to jointly optimize both \mathcal{D}_{Φ} and \mathcal{Q}_{Θ} blocks in the MoDL framework with the goal of improving the reconstruction performance. Specifically, we propose to jointly

learn the sampling pattern Θ and the CNN parameter Φ from training data using

$$\{\Theta^*, \Phi^*\} = \arg \min_{\Theta, \Phi} \sum_{i=1}^N \|\mathcal{M}_{\Theta, \Phi}(\mathcal{A}_{\Theta}(\rho_i)) - \mathbf{x}_i\|_2^2. \quad (10)$$

While the proposed J-MoDL framework (in Fig. 1(b)) can be generalized to other error metrics such as perceptual error, we focus on the ℓ_2 error in this work.

The use of the data consistency term within the MoDL framework makes the parameters of the CNN \mathcal{D}_{Φ} more decoupled from the sampling pattern, compared to the direct-inversion scheme. Specifically, the CNN network \mathcal{D}_{Φ} behaves as a *denoiser* for the specific class of images rather than performing an inversion. We hypothesize that the improved decoupling between the sampling pattern and the CNN parameters translate to a smoother optimization landscape, thus reducing the dependence on the initialization compare to PILOT [22].

F. Parameterization of the sampling pattern

Our initial results involving unconstrained optimization of the sampling patterns had some challenges. Specifically, the final solution was heavily dependent on the initialization of the sampling pattern, similar to [22]. We hence propose to further simplify the optimization landscape by reducing the dimension of the search space. Specifically, we assume that the sampling pattern to be the union of transformed versions of a template set Γ

$$\Theta = \bigcup_{i=1}^P \mathcal{T}_{\theta_i}(\Gamma). \quad (11)$$

Here, \mathcal{T}_{θ_i} is a transformation that is dependent on the parameter θ_i . This model can account for a variety of multi-shot trajectories used in MRI. For instance, one could choose the set Γ as samples on a line, while $\mathcal{T}_{\theta_i}; i = 1, \dots, P$ could denote rotations with angle θ_i ; Θ will essentially be a radial sampling pattern. Similarly, if Γ consists of samples from a spiral trajectory, Θ will correspond to an interleaved multi-shot spiral trajectory. The benefit with this approach is that the sampling set Θ_i is described by the set parameters $\theta = \{\theta_i; i = 1, \dots, P\}$. Thus, the optimization problem (10) simplifies to the search over the continuous parameters Φ and θ .

In this work, we restrict our attention to the optimization of the phase encoding locations in MRI, while the frequency encoding direction is fully sampled. Specifically, we choose Γ as samples on a line and \mathcal{T}_{θ_i} are translations orthogonal to the line. Here, $\theta_i; i = 1, \dots, P$ are the phase encoding locations. In the 2-D setting, we also consider sampling patterns of the form

$$\Theta = \Theta_v \cap \Theta_h, \quad (12)$$

where Θ_v and Θ_h are 1-D sampling patterns in the vertical and horizontal directions, respectively. Here, we assume that the readout direction is orthogonal to the scan plane and is fully sampled. The sampling pattern in this setting is shown in Fig. 5.

In addition to reducing the parameter space, the above Cartesian approaches also simplify the implementation. We focus on this setting because the data consistency blocks denoted by \mathcal{Q}_{Θ} can be implemented in-terms of the 1-D Fourier transform analytically, eliminating the need for non-uniform fast Fourier transform (NUFFT) operators. In our future work, we will consider more general non-Cartesian sampling patterns using the NUFFT.

G. Architecture of the networks used in joint optimization

Figure 1(b) shows the joint model-based deep learning framework (MoDL). The framework alternates between data consistency blocks \mathcal{Q}_{Θ} that depend only on the sampling pattern and the CNN blocks \mathcal{D}_{Φ} . The CNN block is more decoupled from the sampling patterns than the direct-inversion approach in Fig. 1(a). We hypothesize that the increased decoupling between the components translate to improved optimization landscape and hence fewer local minima issues. We unrolled the MoDL algorithm in Fig. 1(b) for $K=5$ iterations (i.e., five iterations of alternating minimization) were used to solve Eq. (4). The forward operator \mathcal{A}_{Θ} is implemented as a 1-D discrete Fourier transform to map the spatial locations to the continuous domain Fourier samples specified by Θ , following the weighting by the coil sensitivities, as described by (1). The data consistency block \mathcal{Q}_{Θ} is implemented using the conjugate gradients algorithm. The CNN block \mathcal{D}_{Φ} is implemented as a UNET with four pooling and unpooling layers. The parameters of the blocks \mathcal{D}_{Φ} and \mathcal{Q}_{Θ} are optimized to minimize (10). We relied on the automatic-differentiation capability of TensorFlow to evaluate the gradient of the cost function with respect to Θ and Φ .

For comparison, we also study the optimization of the sampling pattern in the context of direct-inversion (i.e., when a UNET is used for image inversion). A UNET with the same number of parameters as the MoDL network considered above was used to facilitate fair comparison. This optimization scheme where both sampling parameters and the UNET parameters are learned jointly is termed as J-UNET (Fig. 1(a)).

H. Training strategies

1) *Proposed continuous optimization:* We first considered a random sampling pattern with 4% fully sampled locations in the center of the k-space, and trained only the network parameters Φ . This training strategy is referred to as Φ -alone optimization. Once this training is completed, we fixed the trained network parameters and optimized the sampling locations alone. Specifically, we consider the sampling operator \mathcal{A}_{Θ} and its adjoint as layers of the corresponding networks. The parameters of these layers are the location of the samples, denoted by Θ . We optimize for the parameters using stochastic gradient descent, starting with random initialization of the sampling locations Θ . The gradients of the variables are evaluated using the automatic differentiation capability of TensorFlow. This strategy, where only the sampling patterns are optimized, is referred to as the Θ -alone optimization; here, the parameters of the network derived from the Φ only optimization are held constant. The third strategy, we refer

as Θ , Φ -Joint, simultaneously optimize for both, the sampling parameter Θ as well as the network parameters Φ . The Φ -alone optimization strategy take 5.5 hours during training in single-channel settings as described in section III-B. The Θ -alone and Φ , Θ -joint strategies only takes 1 hour during training with an initialization from Φ -alone model.

2) *Greedy optimization in the single-channel setting [11]*: We implemented the greedy backward selection strategy to learn the sampling pattern in single-channel settings on the knee dataset. The maximum number of reconstructions for an acceleration factor of 4 (i.e., $368/4=92$ lines) needed to implement the greedy approach is $(368-92)/2 \times (368+92) = 63480$ for a 368×640 image. We performed the greedy learning with 10 images which requires one second in the inner MoDL reconstruction algorithm. Therefore, total time to learn the greedy mask with 10 training images is $63480/3600 \approx 17.6$ hours. We utilized Φ -alone MoDL architecture as the reconstruction network inside the Greedy approach. This network was trained with different pseudo-random sampling masks with fully sampled 4% lines in the center.

III. EXPERIMENTS AND RESULTS

A. Datasets

We relied on two datasets for comparison.

1) *Knee dataset*: We used a publicly available parallel MRI knee dataset as in [15]. The training data constituted of 381 slices from ten subjects, whereas test data had 80 slices from two subjects. Each slice in the training and test dataset had different coil sensitivity maps that were estimated using the ESPIRIT [29] algorithm. Since the data was acquired by using a 2-D Cartesian sampling scheme, we relied on a 1-D undersampling of this data.

In the single-channel experiments, we performed a complex combination of the coil images to obtain a single-coil image, which was used in our experiments. We consider the forward model in (1) with $J = 1$ and $s_1(\mathbf{x}) = 1$.

2) *Brain dataset*: Another parallel MRI brain data used for this study were acquired using a 3-D T2 CUBE sequence with Cartesian readouts using a 12-channel head coil. The matrix dimensions were $256 \times 232 \times 208$ with a 1 mm isotropic resolution. Fully sampled multi-channel brain images of nine volunteers were collected, out of which data from five subjects were used for training, while the data from two subjects were used for testing and remaining two for validation. Since the data was acquired with a 3-D sequence, we used this data to determine the utility of 1-D and 2-D sampling in parallel MRI settings. Specifically, we performed a 1-D inverse Fourier transform along the readout direction and considered the recovery of each slice in the volume. Following the image formation model in (1), additive white Gaussian noise of standard deviation $\sigma = 0.01$ was added in k-space in all the experiments.

B. Single Channel Setting

We first consider the single-channel setting as in [10], [11], [20]–[22], where an undersampled Fourier sampling forward operator is considered. Unlike most of the discrete

TABLE I
SINGLE CHANNEL SETTINGS: THE AVERAGE PSNR (dB) AND SSIM VALUES OBTAINED OVER THE TEST DATA OF TWO SUBJECTS WITH TOTAL OF 80 SLICES USING DIFFERENT OPTIMIZATION STRATEGIES AT 4X ACCELERATION.

Optimize	PSNR		SSIM	
	UNET	MoDL	UNET	MoDL
Φ alone	30.00	33.42	0.84	0.85
Θ alone	25.40	35.03	.071	0.89
Greedy	–	36.23	–	0.87
Θ , Φ Joint	30.61	35.69	0.87	0.90

optimization schemes, we consider the optimization of the continuous values of the phase encoding locations $\theta_1, \dots, \theta_P$. We consider an undersampling factor of four.

Table I reports the average PSNR and SSIM values obtained on the test data. The top row corresponds to the optimization of the network parameters Φ alone, assuming incoherent undersampling patterns. The pseudo-random sampling patterns used for initialization were generated following [15], where 4% of the k-space center was fully sampled. We note that the MoDL framework provides an approximate 3.5 dB improvement in performance over a UNET scheme with the same number of parameters in the Φ only setting. This observation is inline with the experiments in [14].

The second row in Table I reports the result of only optimizing the sampling parameter Θ alone while keeping the reconstruction network fixed as trained in row one. We note the performance of the UNET approach degraded in this case. This deterioration can be attributed to the close coupling between the UNET parameters and the sampling pattern in direct-inversion schemes. Specifically, the UNET parameters need to be optimized for each sampling pattern; when the sampling pattern differs from the ones that were used to train the UNET, the performance deteriorates drastically. By contrast, we note that the optimization of the sampling pattern provided a 1.5 dB improvement in performance in the MoDL setting, indicating the improved decoupling offered by the model-based setting.

The third row in Table I corresponds to the optimization of the sampling pattern using the greedy backward selection strategy. The MoDL algorithm was used as the inner reconstruction algorithm, whose parameters Φ were kept fixed during the optimization. The algorithm selects a subset of Cartesian sampling locations using the greedy approach. We observe that the greedy strategy offers a significant improvement in performance over the initialization. The PSNR of the greedy optimization scheme is better than that of the continuous optimization scheme, while the SSIM is marginally lower. A drawback of the greedy strategy is the high computational complexity, which forbids its use in large scale problems and in the parallel MRI setting using multiple images.

The last row of Table I corresponds to the joint optimization scheme, where both Θ and Φ are trained with the initial sampling pattern used in the top row. The resulting J-MoDL scheme offers a 2.27 dB improvement in performance over the case where only the network is trained, which is better by 0.6 dB over the case where only the sampling pattern is optimized.

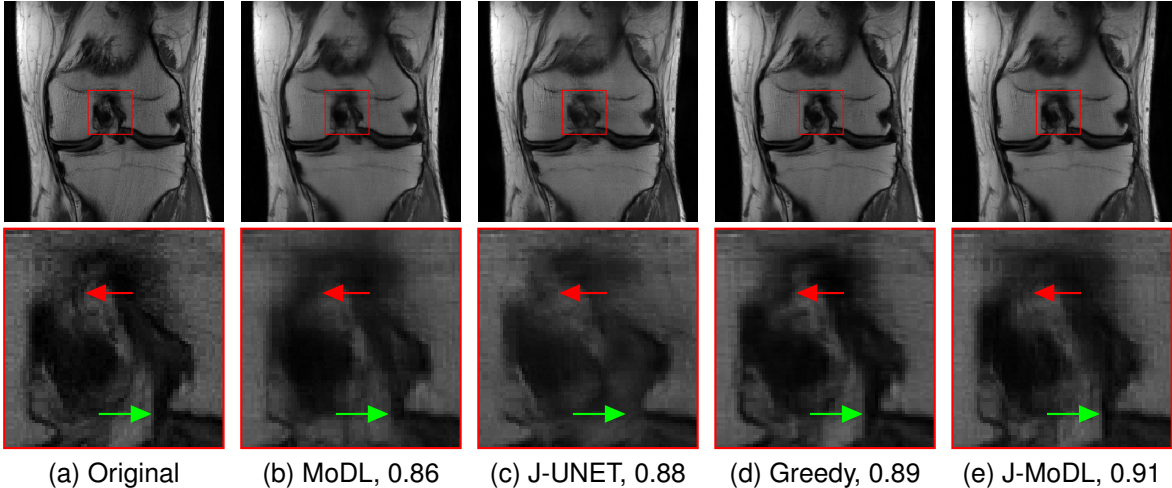


Fig. 2. The visual comparisons of different optimization strategies, described in section III-B, on a test slice. The numbers in the subcaption show the SSIM values. The green arrow in the zoomed area points to a feature not captured by J-UNET despite having higher SSIM as compare to MoDL. The red arrow points to thin vertical features not captured by the Greedy approach.

TABLE II
IMPACT OF OPTIMIZATION STRATEGIES FOR PARALLEL MRI RECOVERY OF KNEE IMAGES USING 1-D SAMPLING. THE RESULTS CORRESPOND TO TWO SUBJECTS WITH A TOTAL OF 80 SLICES.

		PSNR		SSIM	
Acc.	Optimize	UNET	MoDL	UNET	MoDL
4x	Φ alone	29.95	34.21	0.83	0.91
	Θ alone	28.85	37.66	0.86	0.96
	Θ, Φ Joint	34.02	41.28	0.93	0.96
6x	Φ alone	29.24	32.40	0.82	0.89
	Θ alone	24.45	33.31	0.78	0.93
	Θ, Φ Joint	29.62	35.93	0.89	0.93

By contrast, the J-UNET approach provided only a 0.6 dB improvement over the initialization. The results demonstrate the benefit of the decoupling of the sampling pattern and CNN parameters offered by MoDL.

The visual comparisons of these strategies are shown in Fig. 2. The proposed J-MoDL method provides significantly improved results over the MoDL scheme as highlighted by the zoomed region. The improvement offered by the proposed continuous domain optimization scheme is comparable in performance with the greedy algorithm. The optimization of the sampling patterns also improved the UNET performance. However, the results are not as good as the MoDL setting.

Figure 2 also demonstrates the benefits of performing joint optimization of both the sampling pattern and the network parameters (Fig. 2(e)) as compared to the network alone (Fig. 2(b)). The red arrows clearly show that the proposed J-MoDL architecture preserves the high-frequency details better than the MoDL architecture.

C. Parallel Imaging (Multichannel) with 1-D sampling

Table II summarizes the impact of sampling optimization using different strategies in the 1-D parallel MRI setting on knee images. The first row denoted as Φ alone in Table II

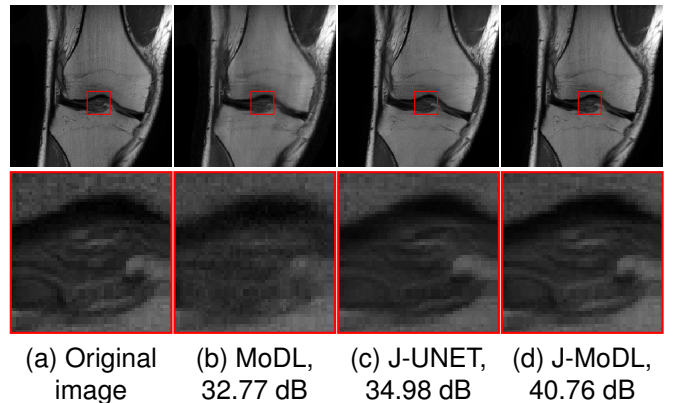


Fig. 3. Comparison of joint and network-alone optimization in parallel imaging settings, described in section III-C, with a 1-D sampling mask. The numbers in subcaptions are showing the PSNR (dB) values. (a) shows a fully sampled image from the test dataset. (b) shows the reconstructed image with a pseudo-random 4x acceleration mask using the MoDL approach. (c,d) shows joint optimization of sampling as well as network parameters using direct-inversion and model-based techniques, respectively. The zoomed areas clearly show that joint learning better preserves the fine details.

corresponds to optimizing the network parameters alone without optimizing the sampling mask. The sampling mask, in this case, is pseudo-random as in the single-channel setting. We observe that the MoDL scheme provides around 4 dB and 3 dB improvement in the 4x and 6x acceleration cases, respectively. We note that both networks use the same number of free parameters. In the second row denoted as Θ alone optimization, only the sampling mask is optimized, while keeping the reconstruction parameters fixed to optimal values as derived in the first row. As in the single-channel setting, we observe that the performance of the UNET declines. We did not use the greedy approach in parallel imaging scheme due to its high computational complexity. The second row corresponds to the optimization of the sampling pattern, while keeping the reconstruction parameters fixed. We note that

TABLE III
IMPACT OF OPTIMIZATION STRATEGIES FOR PARALLEL MRI RECOVERY OF THE BRAIN IMAGES USING 2-D SAMPLING. THE PSNR AND SSIM VALUES ARE REPORTED FOR THE AVERAGE OF 200 SLICES OF TWO TEST SUBJECTS AT 4X, 6X, AND 8X ACCELERATION (ACC.).

Acc.	Optimize	PSNR		SSIM	
		UNET	MoDL	UNET	MoDL
6x	Φ alone	27.78	32.50	0.83	0.92
	Θ alone	29.10	39.86	0.86	0.99
	Θ, Φ Joint	31.48	49.19	0.90	1.00
8x	Φ alone	26.71	31.23	0.80	0.90
	Θ alone	28.07	36.58	0.83	0.97
	Θ, Φ Joint	29.57	40.84	0.86	0.98
10x	Φ alone	26.36	30.29	0.78	0.89
	Θ alone	27.39	37.14	0.81	0.97
	Θ, Φ Joint	28.36	39.16	0.84	0.98

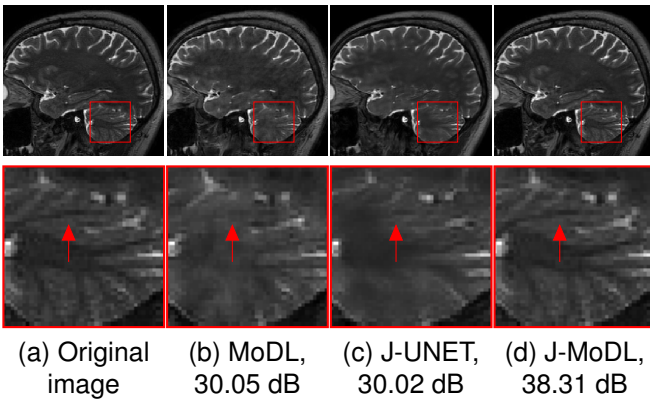


Fig. 4. This figure compares different techniques in parallel imaging settings with a 2-D sampling mask at 8x acceleration as described in section III-D. The J-MoDL approach preserves the fine features in the cerebellum region, as shown by the zoomed area. The red arrow in the zoomed area point to a feature that is well preserved by J-MoDL at 8x acceleration, whereas neither J-UNET nor MoDL preserves it.

the performance of the MoDL framework improves with the optimized sampling pattern. The last row compares joint optimization using direct-inversion and model-based techniques. The J-MoDL PSNR values, on average, are 7 dB higher as compared to the J-UNET method. The results demonstrate the benefit of the decoupling of the sampling and CNN parameters offered by MoDL in the joint optimization strategy.

Figure 3(a) shows an example slice from the test dataset that illustrates the benefit of jointly optimizing both the sampling pattern and the network parameters (Fig. 3(c)) as compared to the network alone in the model-based deep learning framework (Fig. 3(b)). The zoomed image portion shows that joint learning using J-MoDL better preserves the soft tissues in the knee at the four-fold acceleration case in parallel MRI settings.

D. Parallel Imaging (Multichannel) with 2-D sampling

Table III summarizes the comparison results in the multichannel setting with 2-D sampling patterns, as described by (12). Both the direct-inversion based framework (UNET) and the model-based framework (MoDL) are compared in Table III at three different optimization strategies for three

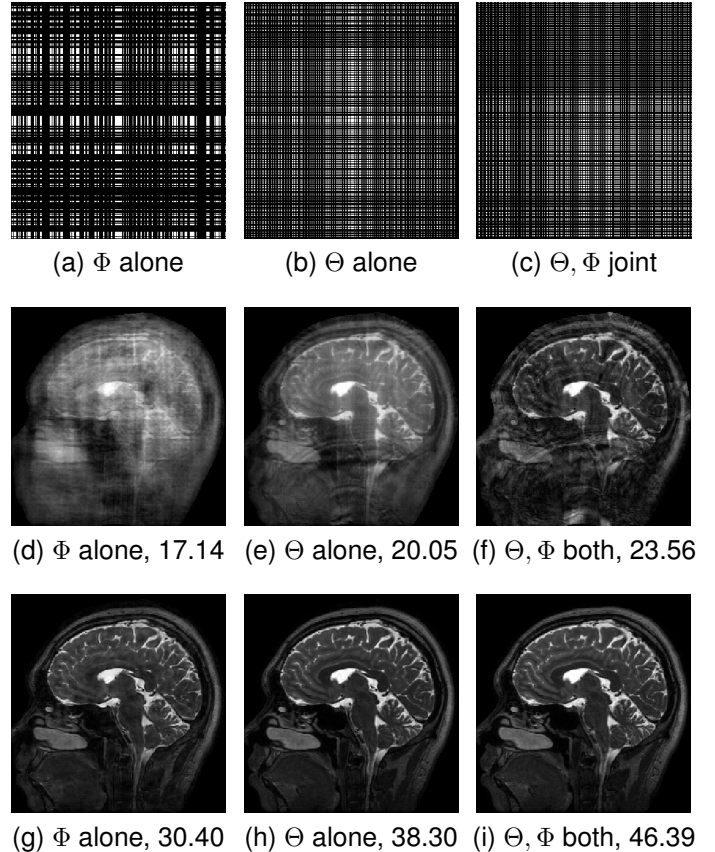


Fig. 5. This figure compares the reconstruction quality obtained by three different optimization strategies in 2-D parallel MRI settings at 6x acceleration as described in section III-D. Rows one, two, and three show masks, $A^H b$, and reconstruction outputs, respectively. The joint optimization of mask and network parameters results in an optimized mask (c) that leads to the best reconstruction quality, as shown in (i).

acceleration factors. The 2-D sampling pattern, together with parallel acquisition, enables us to achieve higher accelerations. The trends of the different methods continue to be the same as in the previous experiments.

The improved performance offered by the optimization of the sampling pattern in 2-D parallel imaging settings can be appreciated from Fig. 4. The zoomed portion in Fig. 4 shows the cerebellum region in which all the fine features are reconstructed well by the proposed J-MoDL approach at 8x acceleration. The red arrow is pointing to a high-frequency feature that is not recovered by the joint learning in the direct-inversion framework (J-UNET). This feature is also not recovered by the fixed model-based deep learning framework without joint optimization (see Fig. 4(b)).

We show the sampling patterns, gridded reconstructions $A_{\Theta}^H(b)$, and the recovered images using the MoDL scheme in Fig. 5. We note that the optimization of the sampling pattern resulted in less aliased gridded reconstructions, which translated to improved MoDL reconstructions. The joint optimization resulted in a more asymmetric pattern. The use of this sampling pattern offered a significant improvement in performance over the other methods. We conjecture that the asymmetric patterns can capitalize on the conjugate symmetry

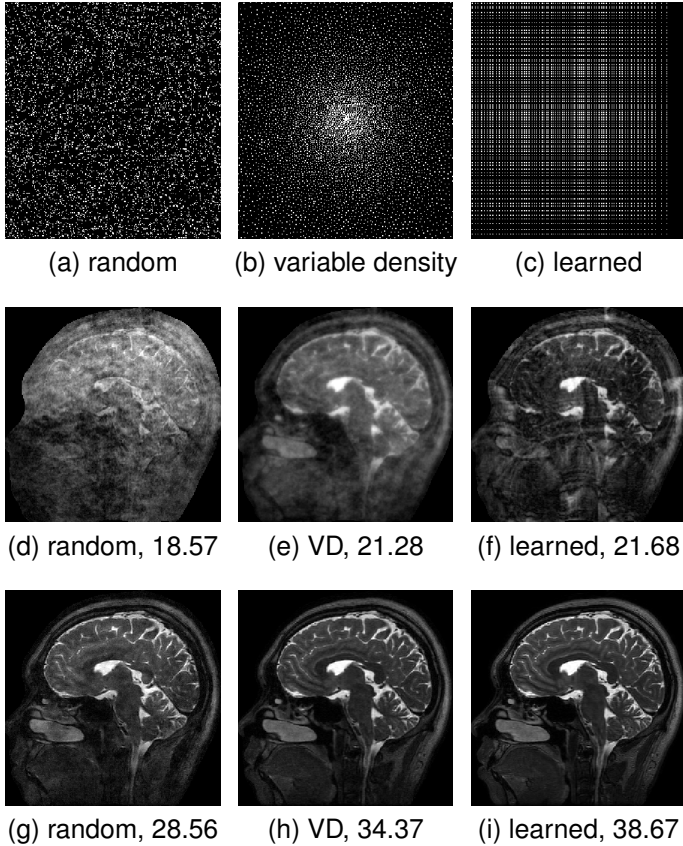


Fig. 6. This figure compares the reconstruction quality obtained by different sampling masks in 2-D parallel imaging settings at 10x acceleration as described in section III-D. Rows one, two, and three shows masks, $A^H b$, and reconstruction outputs, respectively. Two Φ -alone models using the MoDL approach were trained with random masks as well as random variable-density (VD) masks. It can be observed that the learned 2-D mask using the J-MoDL approach outperforms the reconstruction using fixed random and variable-density masks. The numbers in subcaptions are showing PSNR (dB) values.

constraints that are present in MR images with smoothly varying phase, even though we did not explicitly account for this constraint.

E. Comparison with different masks

Figure 6 shows the visual comparison of reconstruction quality obtained with three different sampling patterns at the same 10x acceleration in 2-D parallel MRI settings with the model-based deep learning framework. Figure 6(a) and (b) are showing pseudo-random and variable density (VD) masks, respectively, while Fig. 6(c) shows the learned 2-D mask using joint learning with J-MoDL. These masks result in gridded reconstructions, as shown in Fig. 6(d), (e), and (f). It can be observed from Fig. 6(f) that learned mask results in a gridded reconstruction with comparatively fewer artifacts. Figures 6(g) and 6(h) are the reconstructed images using a fixed mask, whereas Fig. 6(i) corresponds to the reconstruction using joint learning.

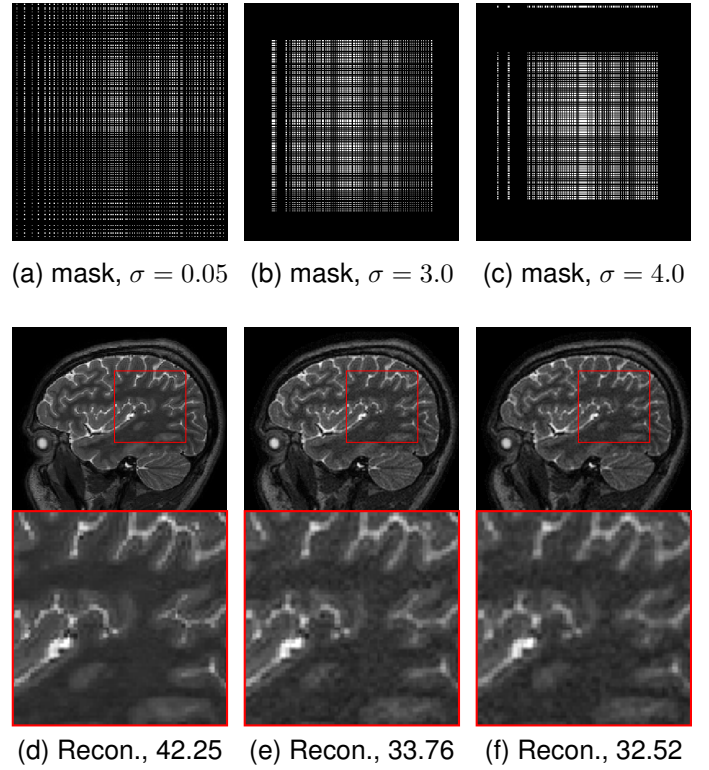


Fig. 7. This figure demonstrates the impact of adding a high amount of noise in the k-space samples in 2-D parallel MRI settings at 8x acceleration as described in section III-D. The first row shows different masks learned with the J-MoDL approach when the Gaussian noise of standard deviation σ is added in the k-space samples. The second row shows corresponding reconstructions (Recon.). Subcaptions of (d), (e), and (f) are showing PSNR (dB) values. As expected, higher noise levels promote the algorithm to learn the sampling parameters that sample more of the low-frequency components from the center of k-space, leading to low-resolution reconstructions.

F. Impact of noise

We study the impact of the adding noise on the learned optimal sampling pattern and the reconstruction performance in Fig. 7. Specifically, we added complex Gaussian noise with different standard deviations to the 8x undersampled k-space measurements. The results show that as the noise standard deviation increase, the optimal sampling patterns get concentrated to the center of k-space. This is expected since the energy of the Fourier coefficients in the center of k-space is higher. As the standard deviation of the noise increases, the outer k-space regions become highly corrupted with noise and hence sampling them do not aid with the reconstruction performance. As expected, the restriction of the sampling pattern to the center of k-space results in image blurring. It can be noted that, during training with different noise levels, no extra constraints were imposed to promote a low-frequency consistency step in the model-based deep learning framework. This experiment empirically shows that the proposed J-MoDL technique indeed conforms with classical model-based techniques while retaining the benefits of deep learning methods.

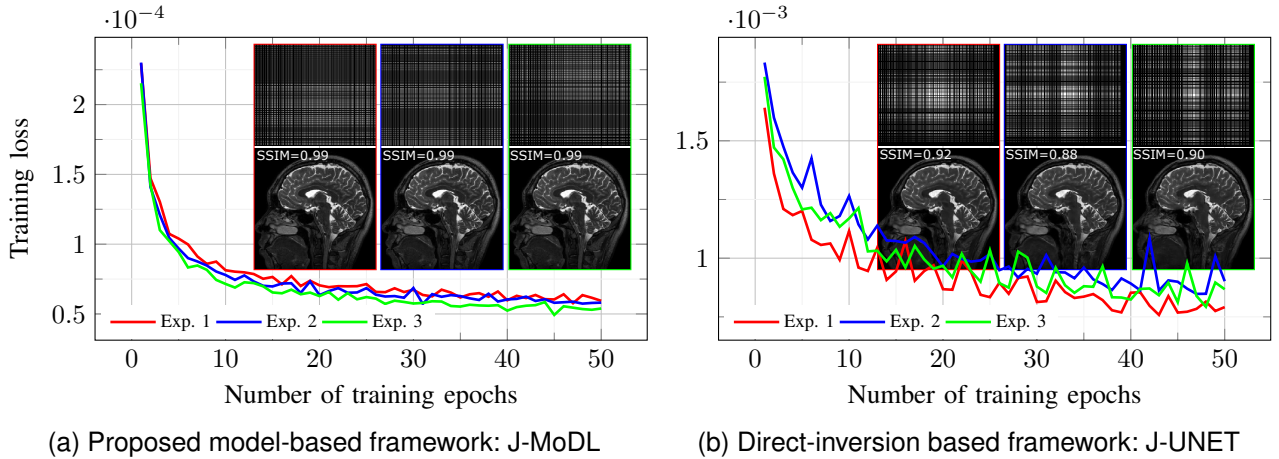


Fig. 8. This figure compares the convergence of training loss in joint optimization with direct-inversion and model-based deep learning frameworks. We performed three independent experiments for each of the two frameworks. The experimental setup for all the three experiments was identical except for the initialization of sampling parameters. The learned masks, reconstructed images, as well as the training loss, are plotted for each of the three experiments. It can be observed that training loss smoothly decays to lower values with the proposed J-MoDL approach as compared to the J-UNET approach.

G. Dependence on Initialization

We study the dependence of both deep learning frameworks on different initializations of the sampling patterns in Fig. 8. We trained both the frameworks with different pseudo-random sampling patterns with the fully sampled center having 4% lines as initialization. The experiments were repeated three times with different initializations. In each experiment, training was performed for 50 epochs.

Figure 8(a) shows the decay of training loss with the proposed J-MoDL scheme, where the sampling pattern is optimized using the MoDL reconstruction network. This figure shows that all the three models converge to nearly the same cost, despite the drastic difference in initialization. The results also show that the unrolled J-MoDL training proceeds relatively smooth despite the problem formulation (4) being highly non-convex. We observe that the final optimal sampling patterns are drastically different. However, the resulting reconstructions are roughly comparable with equivalent SSIM values. We also note that all the sampling patterns show asymmetry (one side of the Fourier domain is sampled predominantly), which shows that all of the networks exploit the conjugate symmetry property.

Figure 8(b) shows similar results with the J-UNET scheme. We observe that the J-UNET scheme converges to relatively different solutions with drastically different reconstruction quality, as shown by SSIM values. It can be noted that the training loss decays to the order of 10^{-3} in J-UNET, whereas it decays to the order of 10^{-4} in the J-MoDL approach.

IV. DISCUSSION AND CONCLUSION

We introduced an approach for the joint optimization of the continuous sampling locations and the reconstruction network for parallel MRI reconstruction. Unlike past schemes, we consider a Fourier operator with continuously defined sampling locations, which facilitated the direct optimization of the sampling pattern. Our experiments show the benefit of using model-based deep learning strategies along with joint

optimization. In particular, the improved decoupling between sampling and the deep network parameters reduces the dependence of the final results on the initialization. In addition, we relied on a parametric sampling pattern with few parameters, which further improved the optimization performance. The experimental results demonstrate the significant benefits in the joint optimization of the sampling pattern in the proposed model-based framework. We will consider extensions to other sampling patterns using a non-uniform fast Fourier transform (NUFFT) as future work.

We constrained the sampling pattern as the tensor-product of two 1-D sampling patterns in this work for simplicity. This approach may be easily generalized to include more general non-Cartesian sampling patterns by using non-uniform fast Fourier transforms. Our work has shown the benefit of using parameterized sampling patterns. Motivated by this approach, we plan to investigate the use of parametric non-Cartesian sampling patterns in the future. The 2-D sampling pattern considered in this work assumed the readouts to be orthogonal to the slice direction. This work may be extended by considering the rotations of a single template as in [30] using non-Cartesian Fourier transforms. Coupled with MoDL reconstruction algorithms, this work is expected to facilitate the recovery of MRI data with higher undersampling rates.

REFERENCES

- [1] D. K. Sodickson and W. J. Manning, "Simultaneous acquisition of spatial harmonics SMASH: fast imaging with radiofrequency coil arrays," *Magnetic resonance in medicine*, vol. 38, no. 4, pp. 591–603, 1997.
- [2] E. Candes and J. Romberg, "Sparsity and incoherence in compressive sampling," *Inverse problems*, vol. 23, no. 3, p. 969, 2007.
- [3] M. Lustig, D. L. Donoho *et al.*, "Compressed sensing MRI," *IEEE signal processing magazine*, vol. 25, no. 2, p. 72, 2008.
- [4] E. Levine, B. Daniel *et al.*, "3D Cartesian MRI with compressed sensing and variable view sharing using complementary Poisson-disc sampling," *Magnetic resonance in medicine*, vol. 77, no. 5, pp. 1774–1785, 2017.
- [5] Y. Gao and S. J. Reeves, "Optimal k-space sampling in MRSI for images with a limited region of support," *IEEE Trans. Med. Imag.*, vol. 19, no. 12, pp. 1168–1178, 2000.

- [6] D. Xu, M. Jacob, and Z. Liang, "Optimal sampling of k-space with Cartesian grids for parallel MR imaging," in *Proc Int Soc Magn Reson Med*, vol. 13, 2005, p. 2450.
- [7] J. P. Haldar and D. Kim, "OEDIPUS: An experiment design framework for sparsity-constrained MRI," *IEEE Trans. Med. Imag.*, 2019.
- [8] E. Levine and B. Hargreaves, "On-the-fly adaptive k-space sampling for linear MRI reconstruction using moment-based spectral analysis," *IEEE Trans. Med. Imag.*, vol. 37, no. 2, pp. 557–567, 2017.
- [9] F. Liu, A. Samsonov *et al.*, "SANTIS: Sampling-augmented neural network with incoherent structure for MR image reconstruction," *Magnetic resonance in medicine*, 2019.
- [10] F. Sherry, M. Benning *et al.*, "Learning the sampling pattern for MRI," *arXiv preprint arXiv:1906.08754*, 2019.
- [11] B. Gözcü, R. K. Mahabadi *et al.*, "Learning-based compressive MRI," *IEEE Trans. Med. Imag.*, vol. 37, no. 6, pp. 1394–1406, 2018.
- [12] H. Chen, Y. Zhang *et al.*, "Low-Dose CT with a Residual Encoder-Decoder Convolutional Neural Network," *IEEE Trans. Med. Imag.*, vol. 36, no. 12, pp. 2524–2535, 2017.
- [13] Y. Han, L. Sunwoo, and J. C. Ye, "k-space deep learning for accelerated MRI," *IEEE Trans. Med. Imag.*, 2019.
- [14] H. K. Aggarwal, M. P. Mani, and M. Jacob, "MoDL: Model based deep learning architecture for inverse problems," *IEEE Trans. Med. Imag.*, vol. 38, no. 2, pp. 394–405, 2019.
- [15] K. Hammernik, T. Klatzer *et al.*, "Learning a Variational Network for Reconstruction of Accelerated MRI Data," *Magnetic resonance in Medicine*, vol. 79, no. 6, pp. 3055–3071, 2017.
- [16] L. Zhang and W. Zuo, "Image Restoration: From Sparse and Low-Rank Priors to Deep Priors," *IEEE Signal Process. Mag.*, vol. 34, no. 5, pp. 172–179, 2017.
- [17] A. Pramanik, H. K. Aggarwal, and M. Jacob, "Off-the-grid model based deep learning O-MoDL," in *IEEE 16th International Symposium on Biomedical Imaging (ISBI)*. IEEE, 2019, pp. 1395–1398.
- [18] H. K. Aggarwal, M. P. Mani, and M. Jacob, "MoDL-MUSSELS: Model-based deep learning for multishot sensitivity-encoded diffusion MRI," *IEEE Trans. Med. Imag.*, 2019.
- [19] M. Mardani, E. Gong *et al.*, "Deep generative adversarial neural networks for compressive sensing MRI," *IEEE Trans. Med. Imag.*, vol. 38, no. 1, pp. 167–179, 2018.
- [20] C. D. Bahadir, A. V. Dalca, and M. R. Sabuncu, "Learning-based optimization of the under-sampling pattern in MRI," in *International Conference on Information Processing in Medical Imaging*. Springer, 2019, pp. 780–792.
- [21] T. Weiss, S. Vedula *et al.*, "Learning fast magnetic resonance imaging," *arXiv preprint arXiv:1905.09324*, 2019.
- [22] T. Weiss, O. Senouf *et al.*, "PILOT: Physics-informed learned optimal trajectories for accelerated MRI," *arXiv preprint arXiv:1909.05773*, 2019.
- [23] K. H. Jin, M. Unser, and K. M. Yi, "Self-supervised deep active accelerated MRI," *arXiv preprint arXiv:1901.04547*, 2019.
- [24] Z. Zhang, A. Romero *et al.*, "Reducing uncertainty in undersampled MRI reconstruction with active acquisition," in *Proceedings of the IEEE Conference on Computer Vision and Pattern Recognition*, 2019, pp. 2049–2058.
- [25] M. Doneva, P. Börnert *et al.*, "Compressed sensing reconstruction for magnetic resonance parameter mapping," *Magnetic Resonance in Medicine*, vol. 64, no. 4, pp. 1114–1120, 2010.
- [26] M. A. T. Figueiredo, R. D. Nowak *et al.*, "An EM Algorithm for Wavelet-Based Image Restoration," *IEEE Trans. Image Process.*, vol. 12, no. 8, pp. 906–916, 2003.
- [27] S. Ma, W. Yin *et al.*, "An Efficient Algorithm for Compressed MR Imaging using Total Variation and Wavelets," in *Computer Vision and Pattern Recognition*, 2008, pp. 1–8.
- [28] M. Jacob, M. P. Mani, and J. C. Ye, "Structured low-rank algorithms: Theory, mr applications, and links to machine learning," *IEEE Signal Processing Magazine*, pp. 1–12, 2019, arXiv preprint arXiv:1910.12162.
- [29] M. Uecker, P. Lai *et al.*, "ESPIRiT - An eigenvalue approach to autocalibrating parallel MRI: Where SENSE meets GRAPPA," *Magnetic Resonance in Medicine*, vol. 71, no. 3, pp. 990–1001, 2014.
- [30] C. Lazarus, P. Weiss *et al.*, "SPARKLING: variable-density k-space filling curves for accelerated T2*-weighted MRI," *Magnetic resonance in medicine*, vol. 81, no. 6, pp. 3643–3661, 2019.